

## Electronic supplementary information

### Lithium-ion storage mechanism in closed pore-rich hard carbon with ultrahigh extra plateau capacity

Chen-Wei Tai<sup>1</sup>, Wen-Yang Jao<sup>1</sup>, Liang-Chieh Tseng<sup>1</sup>, Ping-Chieh Wang<sup>2</sup>, An-Pang Tu<sup>2</sup>, Chi-Chang Hu<sup>1,\*</sup>

<sup>1</sup>Department of Chemical Engineering, National Tsing Hua University, 101, Section 2, Kuang-Fu Road, Hsinchu, 300044, Taiwan

<sup>2</sup>Chang Chun Plastics Co. Ltd., 8, Zhonghua Rd., Hsinchu Industrial Park, Hukou Township 30352, Hsinchu County, Taiwan

\* Corresponding author, e-mail: [cchu@che.nthu.edu.tw](mailto:cchu@che.nthu.edu.tw)

#### Experimental section

##### Synthesis of hard carbon microbeads

The phenolic formaldehyde (PF) resin (CV202 from Chang Chun Group, Taiwan) was cured to form resin spheres by the microwave-induced suspension polymerization. Simply, a mixture contains 1 g phenolic formaldehyde solution (80 wt.% in solvent), 5 wt.% PVA (based on the PF resin mass), and 10-50 wt.% hexamethylenetetramine (HMTA, SHOWA). Then, 20 mL deionized water was added into the above mixture. The final mixture was filled in the reaction tubes sealed with caps, and the whole device was further put into the microwave reactor (CEM discover). The reaction was carried out by microwave-assisted heating at 130°C for 20 min with continuous stirring. After cooling to the ambient temperature, yellow cured resin spheres were clearly suspended in water, and the products were rinsed with acetone to remove excess reactants. Finally, the cured resin spheres were filtered and dried in an oven under vacuum at 80°C for 24 h. The obtained PF resin spheres were carbonized into hard carbon beads at various temperatures for 6 h with a heating rate of 100°C/h in a tube furnace under argon atmosphere.

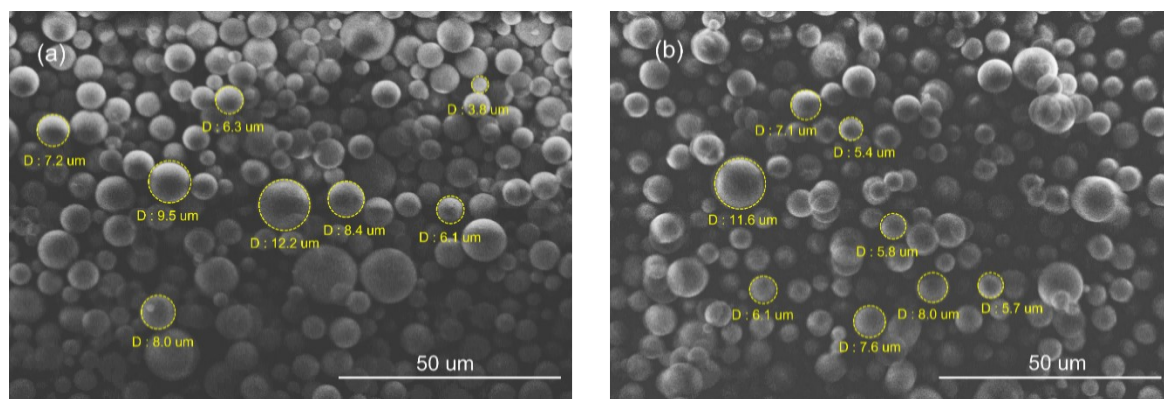
## Material characterization

The morphologies of all samples were examined with a field-emission scanning electron microscope (FE-SEM, Hitachi, SU8010). The high-resolution transmission electron microscopic (HR-TEM) images were recorded on a TEM (JEOL, JEM-2100F). The thermal properties of cured PF resins were examined with a differential scanning calorimeter (Mettler-Toledo, 2-HT) and thermogravimetric analyzer (TGA) (TA instrument, SDT Q600) from room temperature to 1000°C under a heating rate of 10°C/min and nitrogen atmosphere. The chemical structure as well as the bonding environment of cured PF resins were characterized by <sup>13</sup>C CP/MAS solid state NMR (Bruker, AVANCE III-400 MHz solid NMR). The microstructures of samples were characterized by X-ray diffraction (XRD) (Bruker, D8 Advance diffractometer) equipped with a Cu K $\alpha$  radiation source (1.5405 Å) and Raman spectroscopy (PTT, MRID with 532 nm laser beam). The chemical structure analysis was conducted by high-resolution X-ray photoelectron spectroscopy (HRXPS, PHI QuanteraII, ULVAC-PHI). The combustive elemental analyses (C, H, and O) for hard carbons were conducted by the elemental analyzer (Elementar, vario EL cube). N<sub>2</sub>, O<sub>2</sub>, and CO<sub>2</sub> adsorption measurements were conducted on hard carbon samples with surface area and porosity analyzer (Micromeritics, ASAP 2020). Before gas adsorption/desorption analyses, all carbon powder samples were completely degassed at 200°C under high vacuum (< 1  $\mu$ mHg) overnight. The analysis bath temperatures were 77 K for N<sub>2</sub>, 77 K for O<sub>2</sub>, and 273 K for CO<sub>2</sub>, respectively. The specific surface area based on the BET theory were calculated in the relative pressure range from 0.01 to 0.3 P/P<sub>0</sub> for N<sub>2</sub>, from 0.01 to 0.3 P/P<sub>0</sub> for O<sub>2</sub>, and from 0.001 to 0.03 P/P<sub>0</sub> for CO<sub>2</sub>. The pore size distributions (PSDs) were derived from adsorption isotherms of different probing gaseous molecules using 2D-NLDFT heterogeneous surface model for carbon materials based on the assumption of slit pores for N<sub>2</sub>, O<sub>2</sub>, and CO<sub>2</sub> in SAIEUS (Micromeritics).

## Electrode preparation and electrochemical test

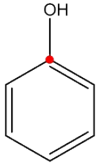
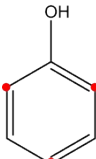
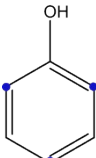
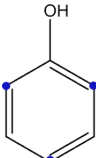
The coating slurry was prepared through a mixture consisting of hard carbon beads, carbon black (XC-72), and polyvinylidene fluoride (PVDF) with the weight ratio of 85:5:10 in N-methyl-2-pyrrolidone (NMP). The slurry was coated on a Cu foil using the doctor blade method with the mass loading of HC beads equal to ca. 2 mg cm<sup>-2</sup>. After coating, the electrodes were dried at 80°C under vacuum for 24 h. The microporous activated carbon (ACS25, provided by China Steel Chemical Corporation, Taiwan) and soft carbon (MGSC, provided by China Steel Chemical Corporation, Taiwan) were fabricated into electrodes following the same procedure.

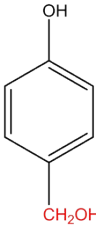
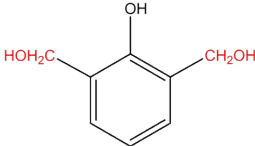
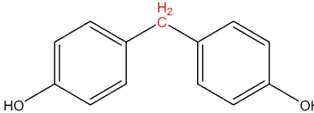
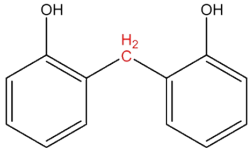
All the electrochemical measurements were conducted in the CR2032 coin cells with a carbon-coated electrode and a lithium foil divided by a glassy fiber (GF/A) as the separator. The supporting electrolyte was a solution of 1 M LiPF<sub>6</sub> in ethylene carbonate (EC), ethyl methyl carbonate (EMC), and dimethyl carbonate (DMC) (1:1:1 in volume). The Karl Fisher (KF) titration coulometer (Metrohm, KF831) was used to confirm the water content in the electrolyte to be below 10 ppm. The electrolyte volume added into all coin cells was fixed to be 100 μL. All the operations were performed in the Argon-filled glove box (H<sub>2</sub>O, O<sub>2</sub> < 0.1 ppm). The cyclic voltammetry and galvanostatic intermittent titration technique (GITT) were respectively conducted on CHI760E (CH instrument, USA) and VMP-3e (BioLogic, France) between 0.001 and 1.5 V (vs. Li<sup>+</sup>/Li) at room temperature. The galvanostatic charge-discharge performance of cells was tested on a Land CT30001A battery test system (Wuhan, China) in the cell voltage range between 0.001 and 1.5 V (vs. Li<sup>+</sup>/Li) at room temperature. For in-situ XRD experiments, the electrochemical test was conducted in an optical cell equipped with a beryllium window (EL-CELL, ECC-Opto-Std).



**Figure S1.** SEM images for cured resin spheres of (a) 10HM and (b) 50HM at the magnification of 1 k.

**Table S1.** Assignments of the  $^{13}\text{C}$  solid state NMR chemical shifts of cured phenolic-formaldehyde resin.

$^{13}\text{C}$ chemical shift (ppm)	Assignments	Reference s
150.0-158.0 (a)	 phenoxy region	1, 2
128.1-130.4 (b)	 substituted para (ortho) position on ring	1, 2
119.5-120.2 (c)	 unsubstituted para position on ring	1, 2
115.0-116.8 (d)	 unsubstituted ortho position on ring	1, 2

75.0-86.6 (e) (f)		Dimethylene ether carbon	3
63.1-65.5 (g)		para methylol	2, 4, 5
58.8-61.6 (h)		ortho methylol	1, 2, 4
53.2-55.8 (i)		sp <sup>3</sup> C-H	3
39.7-41.0 (j)		para-para methylene bridges	5
31.2-32.8 (k)		ortho-ortho methylene bridges	2, 3

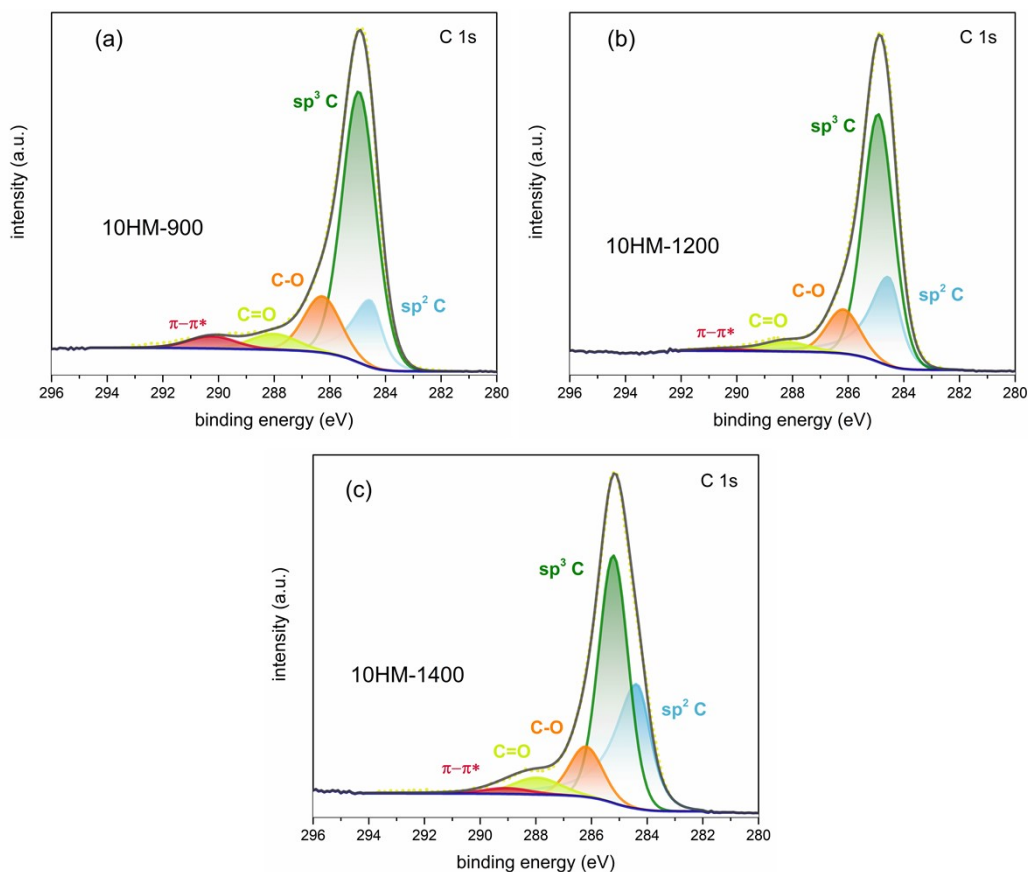


**Figure S2.** The XPS core-level C1s spectra and deconvoluted results of (a) 10HM-900, (b) 10HM-1200, and (c) 10HM-1400.

**Figure S2** display the XPS core-level C1s spectra of HCs, which can be further deconvoluted into five characteristic peaks of  $sp^2$  C (284.5 eV),  $sp^3$  C (284.9 eV), C-O (286.2 eV), C=O (288 eV), and  $\pi-\pi^*$  satellite (290 eV).<sup>6</sup> The detailed results of deconvoluted peaks are summarized in **Table S2**.

**Table S2.** The content of deconvoluted C 1s spectra of 10HM-900, 10HM-1200, and 10HM-1400.

Binding energy (eV)	$sp^2$ C (284.5) (%)	$sp^3$ C (284.9) (%)	C-O (286.2) (%)	C=O (288) (%)	$\pi-\pi^*$ (290) (%)
<b>10HM-900</b>	16.3	60.9	13.9	5.1	3.8
<b>10HM-1200</b>	25.4	59.2	11.5	3.4	0.5
<b>10HM-1400</b>	35.0	47.3	10.8	5.1	1.8

**Table S3.** Microstructural parameters for the synthesized hard carbon beads.

sample	$d_{002}^a$ (nm)	$L_c^b$ (nm)	$N^c$	$L_a^d$ (nm)	$I_{D1}/I_G^e$
10HM-600	0.425	0.79	1.8	2.30	2.13
10HM-900	0.391	0.92	2.3	2.84	2.01
10HM-1200	0.388	0.94	2.4	3.25	1.95
10HM-1400	0.379	1.04	2.7	3.58	1.85

<sup>a</sup> $d_{002}$ : interlayer spacing of pseudo graphitic structure by Bragg's equation:  $\lambda = 2d_{002}\sin\theta$ .

<sup>b</sup> $L_c$ : pseudo graphitic length along the c-axis by Scherrer equation:  $L_c = 0.89\lambda/\beta_c\cos\theta_c$ , where  $\lambda$  is the wavelength of X-ray,  $\beta_c$  is the full width at half maximum of (002) peak, and  $\theta_c$  is the Bragg angle of (002) peak.

<sup>c</sup> $N$ : The number of pseudo graphitic layers estimated via  $L_c/d_{002}$ .

<sup>d</sup> $L_a$ : pseudo graphitic length along the a-axis by Scherrer equation:  $L_a = 1.84\lambda/\beta_a\cos\theta_a$ , where  $\lambda$  is the wavelength of X-ray,  $\beta_a$  is the full width at half maximum of (100) peak, and  $\theta_a$  is the Bragg angle of (100) peak.

<sup>e</sup> $I_{D1}/I_G$ : integrated intensity ratio of D1 and G bands from the deconvoluted Raman spectra.

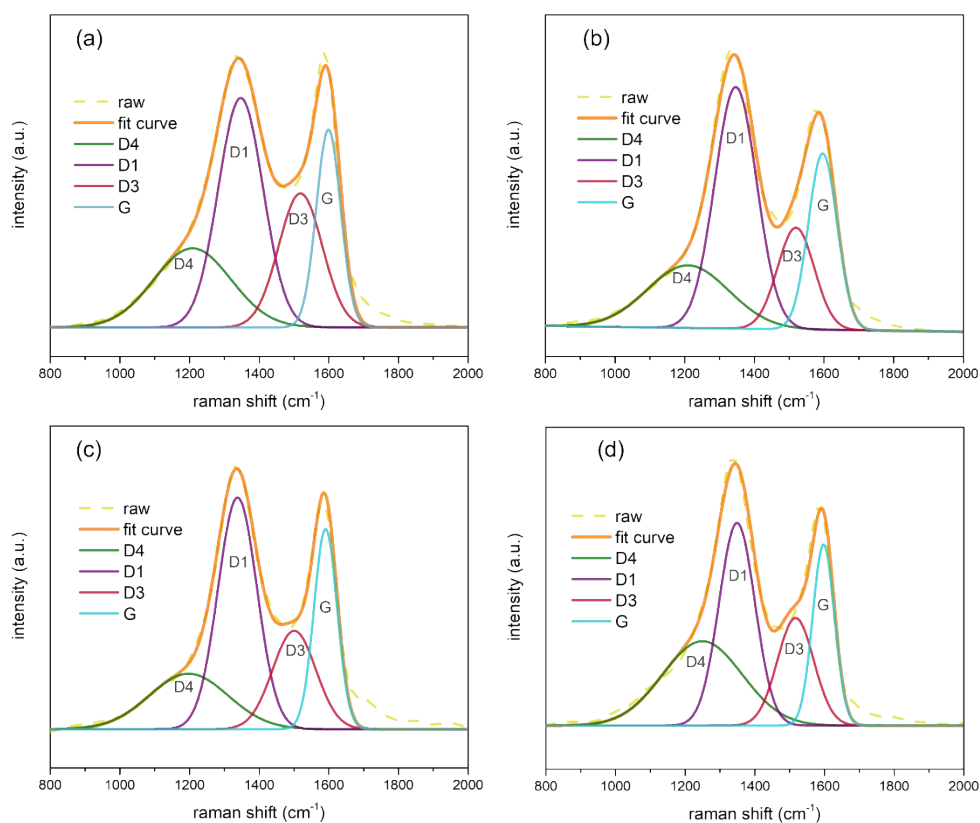


**Figure S3.** The deconvolution curves from Raman spectra of (a) 10HM-600, (b) 10HM-900, (c) 10HM-1200, and (d) 10HM-1400.

All Raman spectra exhibited two peaks nearby  $1360\text{ cm}^{-1}$  (caused by defects) and  $1580\text{ cm}^{-1}$  ( $E_{2g}$  vibration mode of  $sp^2$  carbon). Furthermore, in order to distinguish the disordering degree in these carbon materials, four constituent bands can be specified on these Raman spectra: D4 band ( $1210\text{ cm}^{-1}$ ,  $sp^3$  bonds of C-C stretching), D1 band ( $1350\text{ cm}^{-1}$ ,  $A_{1g}$  symmetry vibration mode caused by defects), D3 band ( $1520\text{ cm}^{-1}$ , amorphous  $sp^2$  bonds of C=C stretching), and G band ( $1600\text{ cm}^{-1}$ , graphitic structure in carbon material)<sup>7</sup>. Here the intensity ratio of  $I_{D1}/I_G$  is employed as the criterion to determine the disordering degree of carbon materials.



**Table S4.** Closed pore volume of the prepared HC and other reported HCs.

Hard carbon	Closed pore volume ( $\text{cm}^3 \text{g}^{-1}$ )	Measurement techniques	Reference
10HM-900	0.336	$\text{N}_2$ , $\text{O}_2$ , and $\text{CO}_2$ adsorptions	this work
HAB-1300	0.124	$\text{N}_2$ , $\text{O}_2$ , and $\text{CO}_2$ adsorptions	8
Glu	0.084	He replacement method	9
A300-1100	0.055	He replacement method	10
CC-1600	0.290	He replacement method	11
HC-325-9	0.062	He replacement method	12

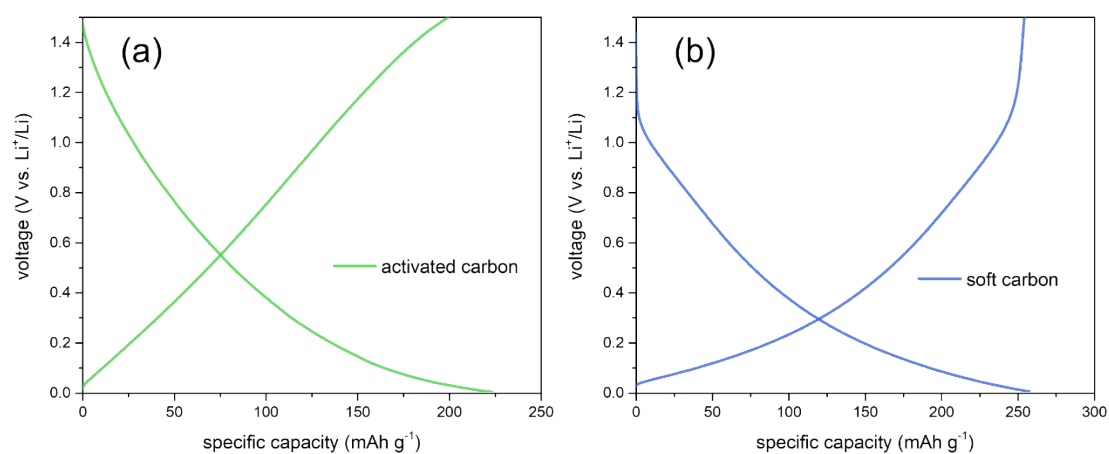


**Figure S4.** Typical galvanostatic charge-discharge (GCD) curves at the current density of  $50 \text{ mA g}^{-1}$  for (a) microporous activated carbon and (b) soft carbon.

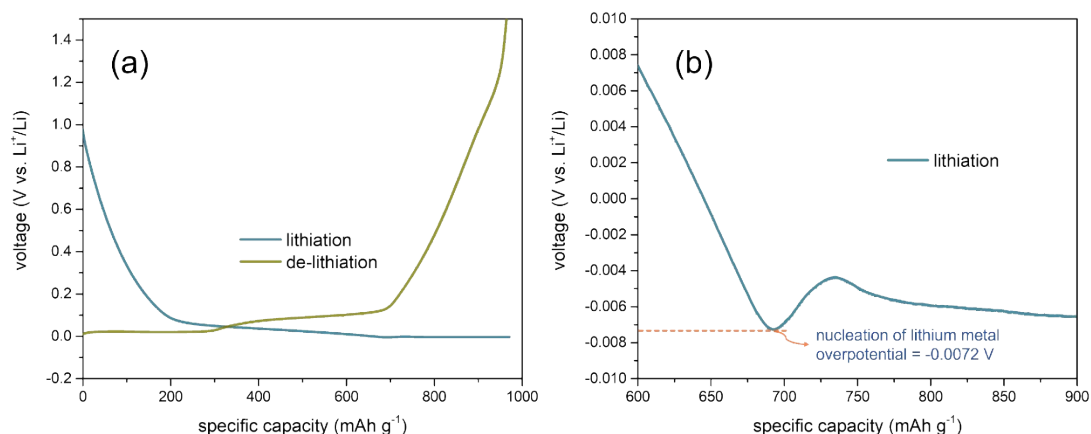


**Figure S5.** (a) Galvanostatic charge-discharge (GCD) curves of 10HM-900 at the current density of  $30 \text{ mA g}^{-1}$  with the voltage range extending to the negative region where the reactions of lithium plating/stripping are initiated. (b) The process of lithium metal nucleation in hard carbon with the nucleation overpotential indicated.

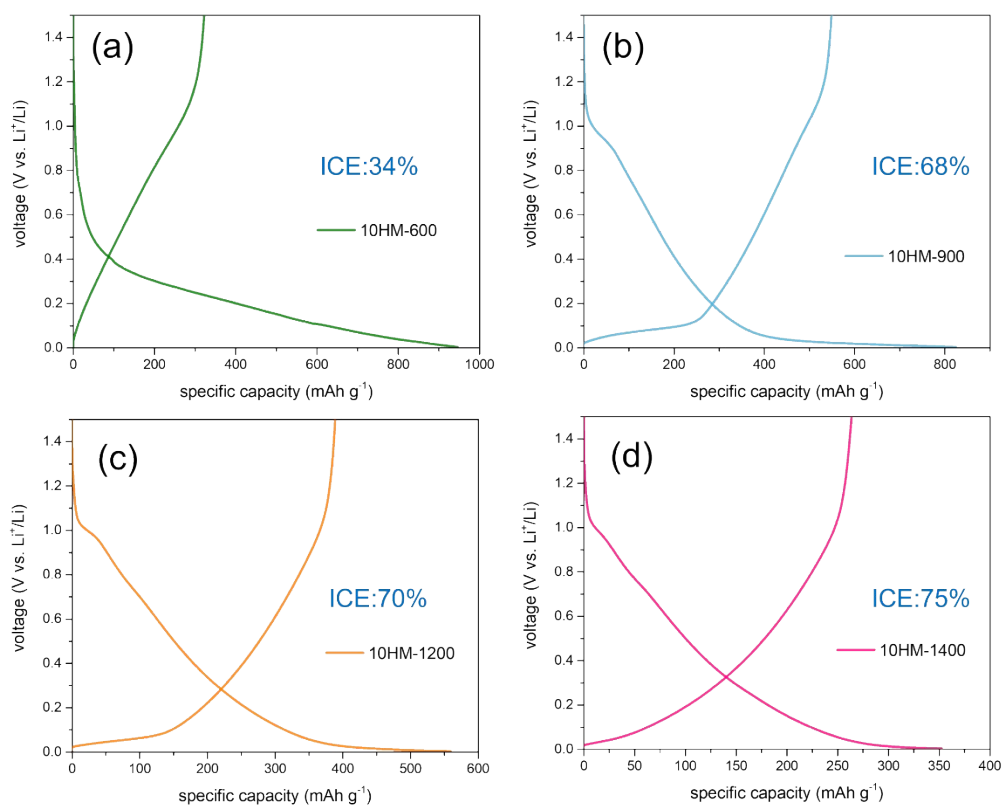


**Figure S6.** Galvanostatic charge-discharge (GCD) curves in the initial cycle at the current density of  $50 \text{ mA g}^{-1}$  for (a) 10HM-600, (b) 10HM-900, (c) 10HM-1200, and (d) 10HM-1400.

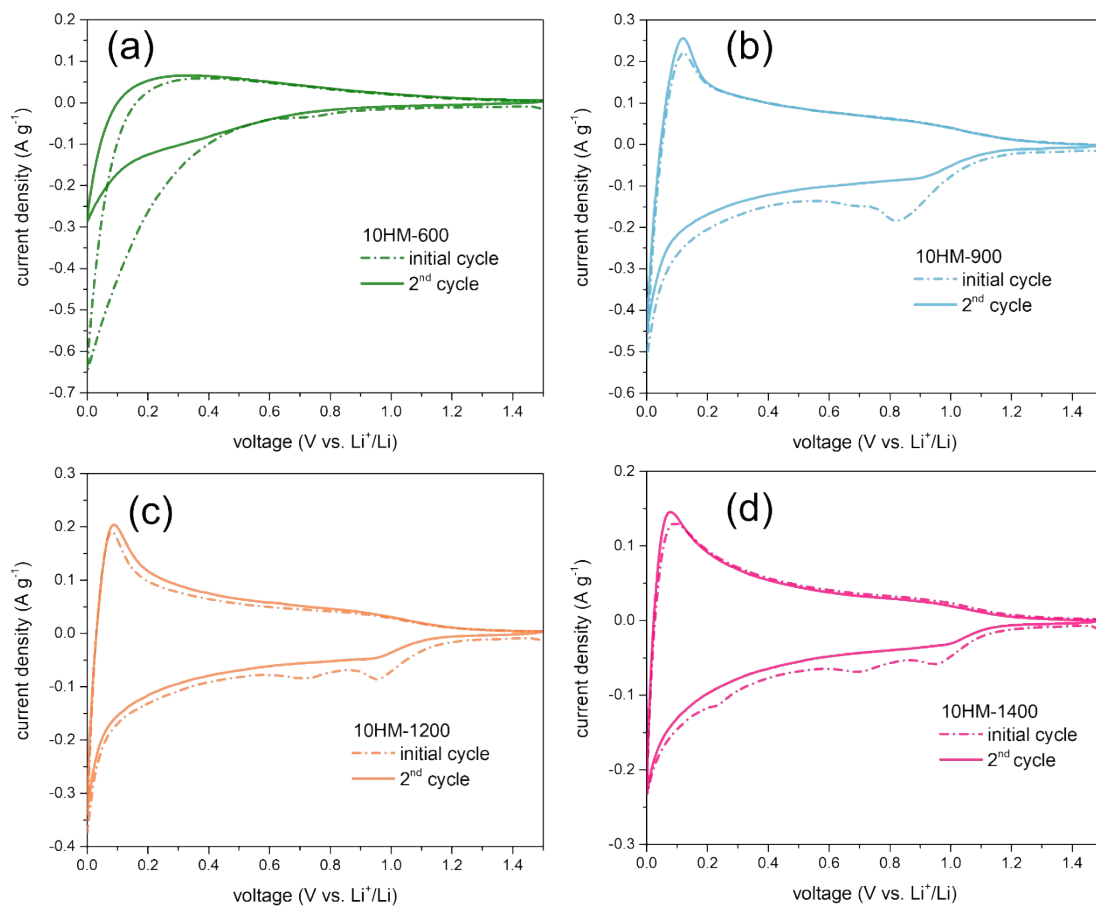


**Figure S7.** Cyclic voltammograms in the initial and the second cycles at a scan rate of  $0.1 \text{ mV s}^{-1}$  for (a) 10HM-600, (b) 10HM-900, (c) 10HM-1200, and (d) 10HM-1400.

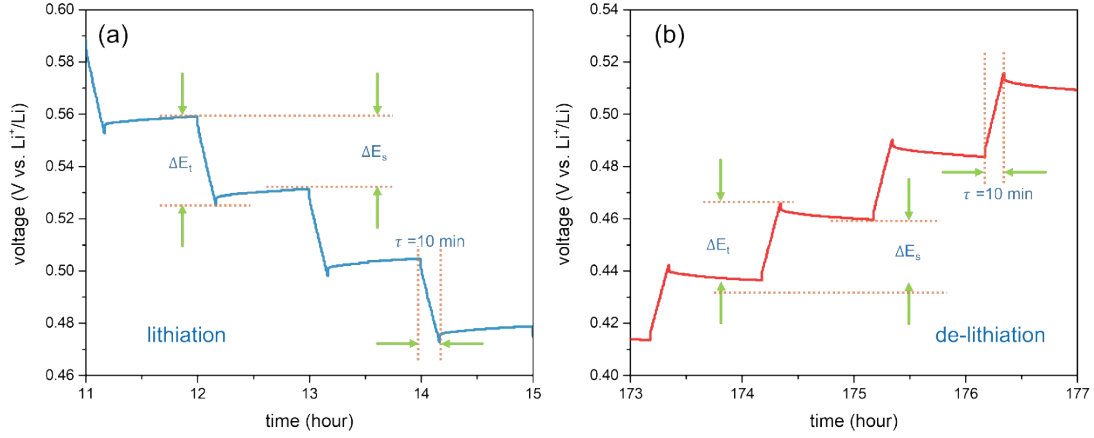


**Figure S8.** Illustration of typical single step GITT profiles to determine  $\Delta E_s$  and  $\Delta E_t$  during (a) lithiation and (b) de-lithiation processes.

The GITT tests for various HCs were conducted at a pulse current of  $30 \text{ mA g}^{-1}$  for 10 min with a relaxation time of 50 min. Based on the Fick's second law of diffusion, the diffusion coefficient of ions ( $D$ ) can be estimated at each single step using the following equation:<sup>13-15</sup>

$$D = \frac{4}{\pi} \left( \frac{iV_m}{zFS} \right)^2 \left[ \frac{\left( \frac{dE}{d\delta} \right)}{\frac{dE}{d\sqrt{t}}} \right]^2 \quad (1)$$

where  $i$  is the current (A);  $V_m$  is the molar volume of active material ( $\text{cm}^3 \text{ mol}^{-1}$ );  $z$  is the charge number;  $F$  is the Faraday constant ( $96485 \text{ C mol}^{-1}$ );  $S$  is the contact area of electrode with electrolyte ( $\text{cm}^2$ );  $dE/d\delta$  is the slope of the coulometric titration curve obtained from the steady-state voltage plot after each titration step;  $dE/d\sqrt{t}$  is the slope of the linearized plot of the potential during the current pulse duration. Furthermore, if sufficient small currents with short time intervals are used,  $dE/d\sqrt{t}$  can be considered to be linear and the coulometric titration curve can be regarded to be linear over the range involved in the step. Then, equation (1) can be simplified as:

$$D = \frac{4}{\pi\tau} \left( \frac{n_m V_m}{S} \right)^2 \left( \frac{\Delta E_s}{\Delta E_t} \right)^2 \quad (2)$$

where  $n_m$  is the mole of the active material, which can be obtained from the mass of

hard carbon beads divided by the molar mass of carbon ( $12 \text{ g mol}^{-1}$ );  $V_m$  is the molar volume of material ( $8 \text{ cm}^3 \text{ mol}^{-1}$ );  $S$  is the contact area of the electrode ( $0.78 \text{ cm}^2$ );  $\tau$  is the pulse duration time (10 min);  $\Delta E_s$  is the steady-state voltage change, and  $\Delta E_t$  is the voltage change during the current pulse application. Note that  $\Delta E_s$  and  $\Delta E_t$  were determined from each pulse and relaxation steps of GITT profiles as illustrated in **Figure S8** for both lithiation and de-lithiation processes.

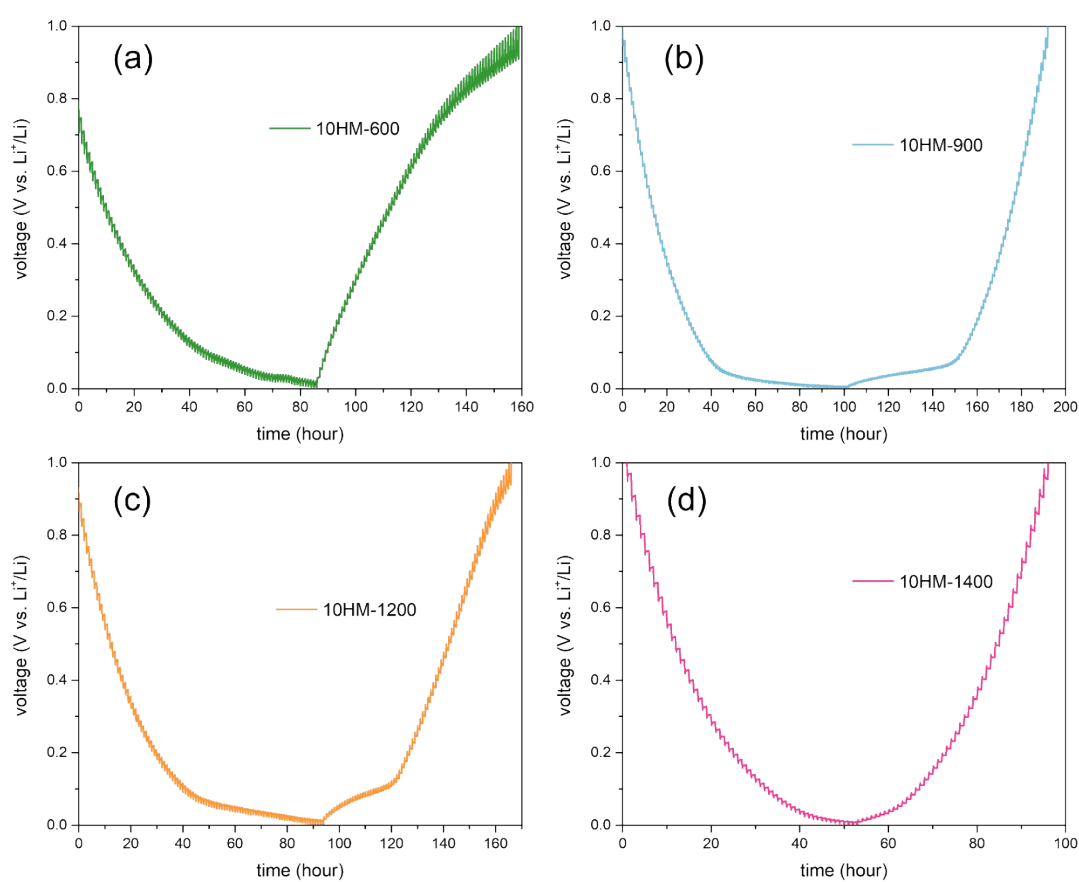


**Figure S9.** The voltage-time profiles of galvanostatic intermittent titration technique (GITT) for (a) 10HM-600, (b) 10HM-900, (c) 10HM-1200, and (d) 10HM-1400 at a pulse current of  $30 \text{ mA g}^{-1}$  for 10 min with rest intervals of 50 min.

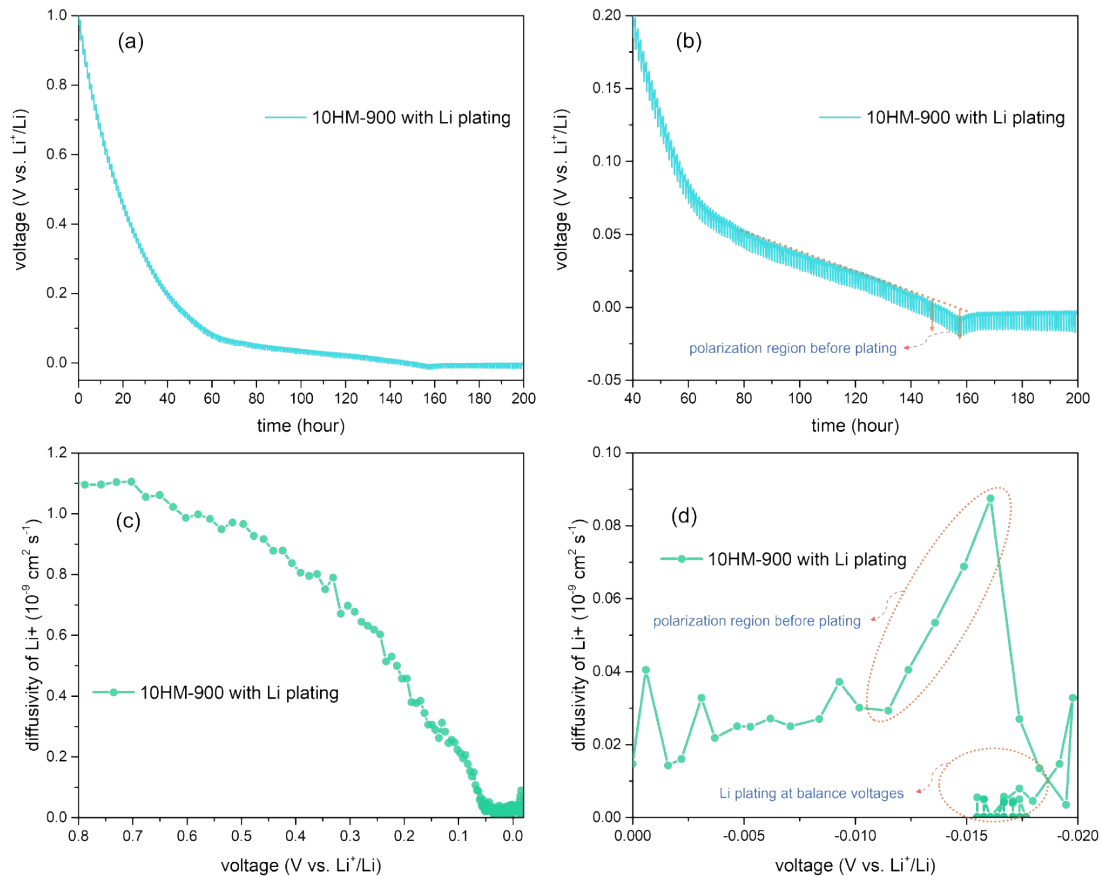


**Figure S10.** (a) The voltage-time profile of galvanostatic intermittent titration technique (GITT) for 10HM-900 with the voltage range extended to the negative region where the reaction of lithium plating is also initiated. (b) A magnification on the low voltage range of the GITT profile where the polarization region before plating is indicated. (c) Lithium-ion diffusion coefficients estimated from the above GITT profile. (d) Lithium-ion diffusion coefficients in the low voltage range where the polarization region before plating and the region of lithium plating at the balance voltage are pointed out.

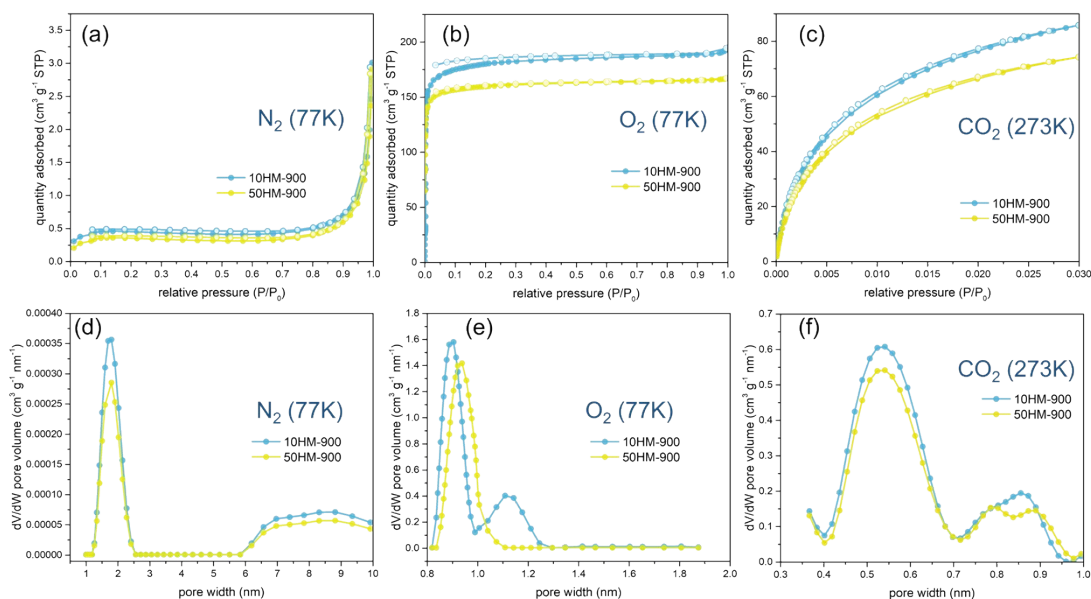


**Figure S11.** Adsorption/desorption isotherms for 10HM-900 and 50HM-900 probed with the adsorbate gas of (a) N<sub>2</sub> (77K), (b) O<sub>2</sub> (77K), and (c) CO<sub>2</sub> (273K) where the solid symbols indicate adsorption, and the open symbols represent desorption. The 2D-NLDFT pore size distributions based on the isotherms of (d) N<sub>2</sub> (77K), (e) O<sub>2</sub> (77K), and (f) CO<sub>2</sub> (273K).

**Table S5.** Textural properties of 10HM-900 and 50HM-900 determined by multiple gas adsorptions.

Sample	SSAN <sub>2</sub> <sup>a</sup> (m <sup>2</sup> g <sup>-1</sup> )	SSAO <sub>2</sub> <sup>b</sup> (m <sup>2</sup> g <sup>-1</sup> )	SSACO <sub>2</sub> <sup>c</sup> (m <sup>2</sup> g <sup>-1</sup> )	V <sub>t</sub> N <sub>2</sub> <sup>d</sup> (cm <sup>3</sup> g <sup>-1</sup> )	V <sub>t</sub> O <sub>2</sub> <sup>e</sup> (cm <sup>3</sup> g <sup>-1</sup> )	V <sub>CO<sub>2</sub>&lt;0.7</sub> <sup>f</sup> (cm <sup>3</sup> g <sup>-1</sup> )	V <sub>closed</sub> <sup>g</sup> (cm <sup>3</sup> g <sup>-1</sup> )
10HM-900	1	483	433	0.004	0.224	0.116	0.336
50HM-900	1	425	391	0.003	0.190	0.094	0.281

<sup>a</sup> SSAN<sub>2</sub>: specific surface area derived from N<sub>2</sub> adsorption.

<sup>b</sup> SSAO<sub>2</sub>: specific surface area derived from O<sub>2</sub> adsorption.

<sup>c</sup> SSACO<sub>2</sub>: specific surface area derived from CO<sub>2</sub> adsorption.

<sup>d</sup> V<sub>t</sub>N<sub>2</sub>: total pore volume detected with N<sub>2</sub> adsorption.

<sup>e</sup> V<sub>t</sub>O<sub>2</sub>: total pore volume detected with O<sub>2</sub> adsorption.

<sup>f</sup> V<sub>CO<sub>2</sub><0.7</sub>: pore volume with size < 0.7 nm detected with CO<sub>2</sub> adsorption.

<sup>g</sup> V<sub>closed</sub>: closed pore volume estimated by the equation: (V<sub>t</sub>O<sub>2</sub> - V<sub>t</sub>N<sub>2</sub>) + V<sub>CO<sub>2</sub><0.7</sub>.

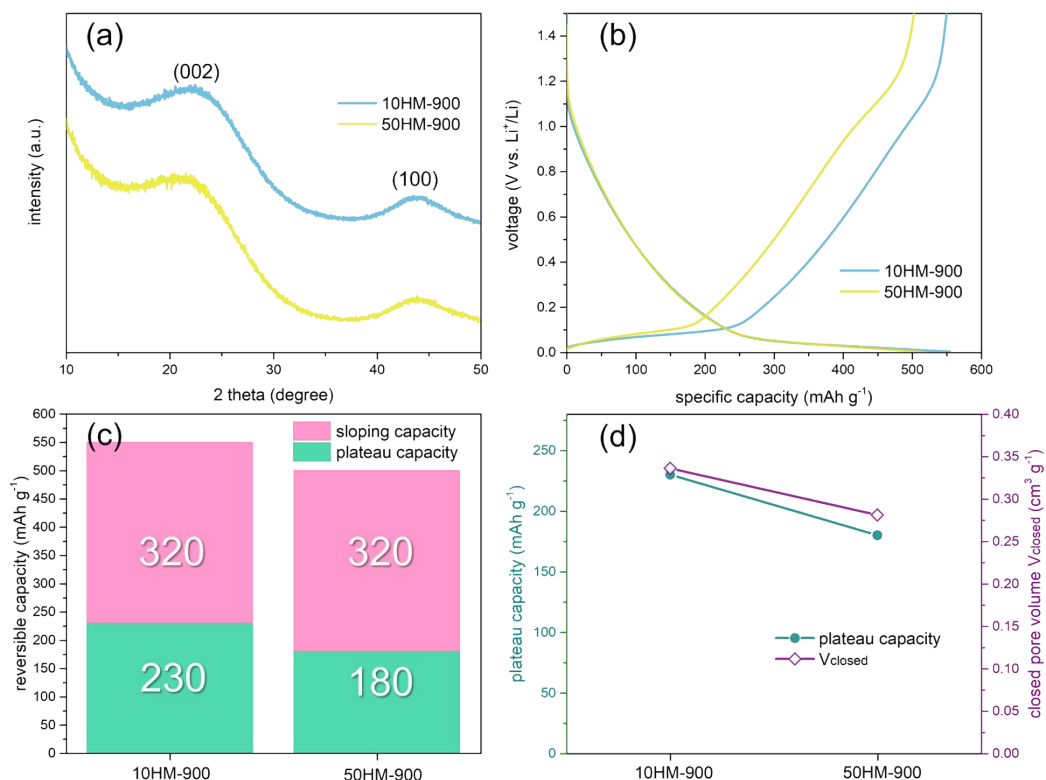


**Figure S12.** Comparisons of 10HM-900 and 50HM-900 in various properties. (a) X-ray diffraction patterns, (b) typical GCD curves at the current density of 50 mA g<sup>-1</sup>, (c) reversible capacities contributed from the sloping and the plateau regions, and (d) the relation between plateau capacities and closed pore volume ( $V_{\text{closed}}$ ).

To investigate the impact of cross-linking degree on the performance of the resulting hard carbons, another cured resin sphere of 50HM was also carbonized into hard carbon beads at 900°C, denoted as 50HM-900. Various properties of 50HM-900 were compared with those of 10HM-900. **Figure S12a** presents the X-ray diffraction patterns of them, and typical diffraction features of amorphous carbons with broad peaks indicating (002) and (100) facets could be observed in both HCs. However, no obvious differences could be demonstrated by XRD results, revealing that the lattice formation is independent of the cross-linking degree. In addition, the porosity of 50HM-900 was detected with multiple gas adsorption (N<sub>2</sub>, O<sub>2</sub>, and CO<sub>2</sub>) because the porosity is the crucial factor in determining the electrochemical performance of HC. The results are displayed in **Figure S11**, and the derived textural property is listed in **Table S5**.



Apparently, according to the multiple gas adsorption detection, the pore category of 50HM-900 can be classified as the closed porosity because it shows type III isotherms with N<sub>2</sub> while type I isotherms with O<sub>2</sub>. Nevertheless, when comparing its porosity with 10HM-900, the decline in SSAO<sub>2</sub>, V<sub>t</sub>O<sub>2</sub>, SSACO<sub>2</sub>, and VCO<sub>2</sub> < 0.7 were observed. This indicates the smaller closed pore volume in 50HM-900 (0.281 cm<sup>3</sup> g<sup>-1</sup>) than that in 10HM-900 (0.336 cm<sup>3</sup> g<sup>-1</sup>). As a result, from the GCD curves in **Figure S12b**, the reversible capacity of 50HM-900 decreases to 500 mAh g<sup>-1</sup> in comparison with 550 mAh g<sup>-1</sup> of 10HM-900, and the main difference originates from the reduced plateau capacity as shown in **Figures S12c** and **S12d**. Therefore, the outcomes suggest that a high cross-linking degree of organic precursors does not favor the formation of closed pores during carbonization and further deteriorates the electrochemical performance due to its high dependence on porosity.

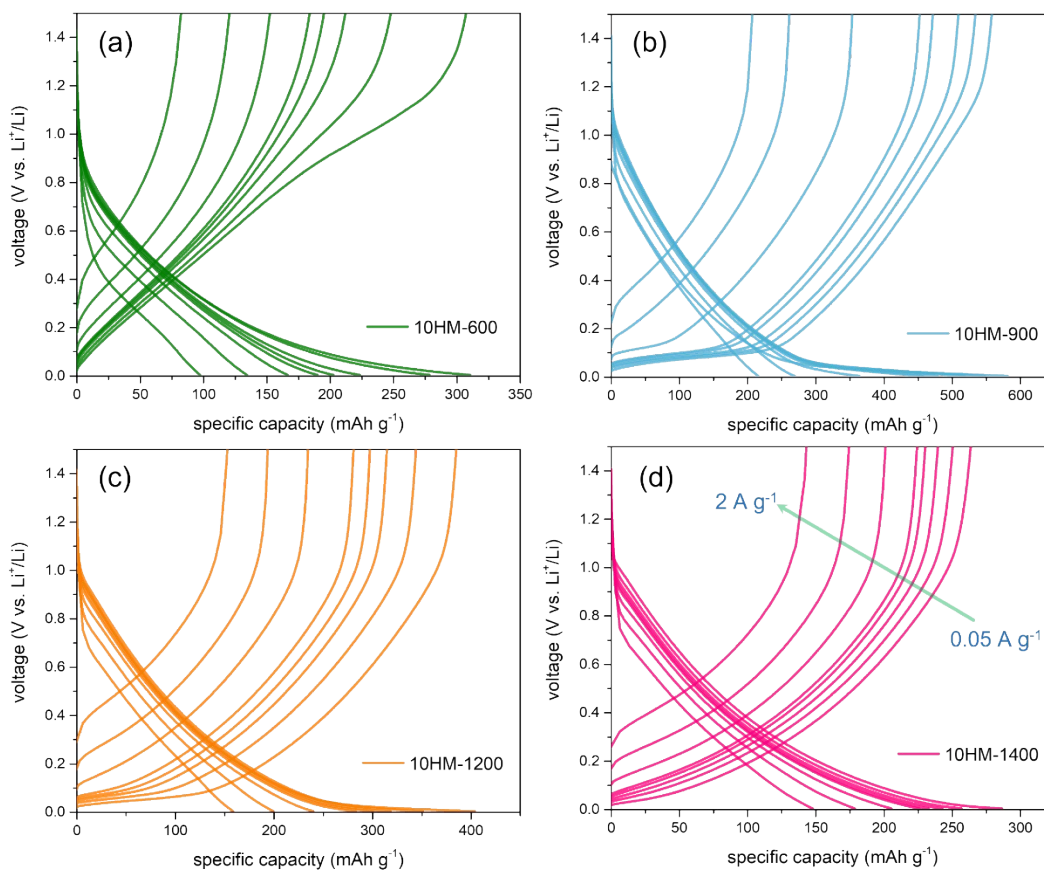


**Figure S13.** Typical galvanostatic charge-discharge (GCD) curves at various current densities from 0.05 to 2 A g<sup>-1</sup> for (a) 10HM-600, (b) 10HM-900, (c) 10HM-1200, and (d) 10HM-1400.

**Table S6.** The C, H, and O analyses of hard carbons by the elemental analyzer using Acetanilide as standard.

	C (%)	H (%)	O (%)
10HM-600	89.9	2.6	7.5
10HM-900	94.1	1.1	4.8
10HM-900-H <sub>2</sub>	96.4	0.8	2.8
10HM-1200	96.8	0.6	2.6
10HM-1400	97.2	0.7	2.1

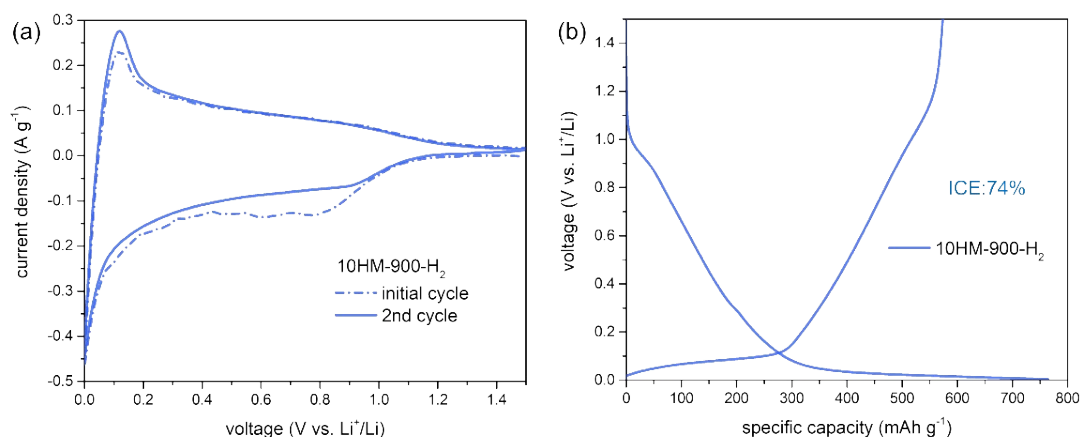


**Figure S14.** (a) Cyclic voltammograms in the initial and the second cycles at a scan rate of 0.1 mV s<sup>-1</sup> and (b) initial GCD curve at 50 mA g<sup>-1</sup> for 10HM-900-H<sub>2</sub>.

The low-temperature hydrogen treatment was performed by the two-stage carbonization. Initially, the 10HM cured PF resin was carbonized in a mixed atmosphere comprising 90% Ar and 10% H<sub>2</sub> in volume, with the temperature rising from room temperature to 300°C at a rate of 100°C/h. The temperature was then held at 300°C for one hour, after that, the gas flow was switched to pure Ar. The temperature was further increased to 900°C at a rate of 100°C/h. Following a 6-h duration at 900°C, the two-stage carbonization process was completed.

**Table S7.** The electrochemical performance of HC beads synthesized in this work and other reported HC materials for lithium-ion storages.

<b>Hard carbon</b>	<b>Current density</b>	<b>ICE (%)</b>	<b>Reversible capacity below 1.5 V (mAh g<sup>-1</sup>)</b>	<b>Plateau capacity below 0.1 V (mAh g<sup>-1</sup>)</b>	<b>Ref.</b>
mildly cured PF resin 10HM-900-H <sub>2</sub>	50 mA g <sup>-1</sup>	74	550	230	this work
sweet gum SGHC-1000	50 mA g <sup>-1</sup>	54	375	0	16
orange peel OPDHC-A	50 mA g <sup>-1</sup>	24	200	0	17
lignin-melamine resins CLM-Ni	100 mA g <sup>-1</sup>	36	250	0	18
lignin LK-200-1350	20 mA g <sup>-1</sup>	62	250	0	19
Sucrose/graphene oxide GH5-1000	50 mA g <sup>-1</sup>	47	350	0	20
PAN CMS1000	100 mA g <sup>-1</sup>	66	250	0	21
water-based alkyd resin PC-800	200 mA g <sup>-1</sup>	53	400	0	22
lignin HC-1300	50 mA g <sup>-1</sup>	73	220	0	23
Carbotron S(F), Kureha Co.	20 mA g <sup>-1</sup>	75	360	0	24
Glucose Glu	20 mA g <sup>-1</sup>	65	170	0	9
unburned charcoal UC-1200	50 mA g <sup>-1</sup>	50	250	0	25
cellulose	20 mA g <sup>-1</sup>	40	320	0	26
biomass-derived char	100 mA g <sup>-1</sup>	38	300	0	27
loofah sponge	100 mA g <sup>-1</sup>	--	420	0	28
garlic peel	100 mA g <sup>-1</sup>	25	380	0	29
BTR New Energy Materials Inc.	0.1C	75	290	0	30
lignocellulosic biomass LSHC-P200	50 mA g <sup>-1</sup>	35	480	0	31
graphite-derived HCDG-3	100 mA g <sup>-1</sup>	36	400	0	32
sodium alginate NGHC	50 mA g <sup>-1</sup>	16	300	0	33
spruce	0.1C	52	210	0	34

polybenzo[ <i>c</i> ]thiophene SM-SDHC700	20 mA g <sup>-1</sup>	34	430	0	35
chitosan CoP@NPHC	100 mA g <sup>-1</sup>	27	400	0	36
Kuraray carbotron P(J)	50 mA g <sup>-1</sup>	77	234	0	37
Fullerene-derived HC C <sub>60</sub> -800	50 mA g <sup>-1</sup>	--	230	0	38
sepia nanosphere DNC-1000	50 mA g <sup>-1</sup>	45	450	0	39

### Space-filling model

The space-filling model calculates the capacity attributed to the filling of ultra-micropores by assuming that alkali metal ions occupies all the ultramicropores.<sup>23</sup> To determine the amount of alkali metal present in the ultramicropores, the model employs the density of 0.53 g cm<sup>-3</sup> for Li metal. The model estimates the capacity by taking into account the atomic mass of the alkali metal, Faraday constant, ultra-micropore volume, and density. Therefore, the capacity can be estimated by the following equation:

$$capacity (mAh g_{carbon}^{-1}) = \frac{V_m \rho F}{3.6M}$$

where  $V_m$  is the ultramicropore volume (cm<sup>3</sup> g<sub>carbon</sub><sup>-1</sup>);  $\rho$  is the density of Li (g<sub>Li</sub> cm<sup>-3</sup>);  $F$  is the Faraday constant (C mol<sup>-1</sup>);  $M$  is the atomic mass of Li (g<sub>Li</sub> mol<sup>-1</sup>)

### References

1. W. Gao, Iranian Polymer Journal, 2012, **21**, 283-288.
2. Z. Yi, J. Zhang, S. Zhang, Q. Gao, J. Li and W. Zhang, Polymers, 2016, **8**, 159.
3. G. E. Maciel, I. S. Chuang and L. Gollob, Macromolecules, 1984, **17**, 1081-1087.
4. B. D. Park and B. Riedl, J. Appl. Polym. Sci., 2000, **77**, 841-851.
5. R. Rego, P. J. Adriaensens, R. A. Carleer and J. M. Gelan, Polymer, 2004, **45**, 33-38.
6. D. J. Morgan, C, 2021, **7**, 51.
7. J. He, C. Zou, J. Zhao, J. Xi, Y. She, M. Ren and Y. Xu, Energies, 2022, **15**, 5627.
8. A. Beda, C. Vaultot and C. Matei Ghimbeu, Journal of Materials Chemistry A, 2021, **9**, 937-943.
9. X. Chen, J. Tian, P. Li, Y. Fang, Y. Fang, X. Liang, J. Feng, J. Dong, X. Ai, H.

- Yang and Y. Cao, *Advanced Energy Materials*, 2022, **12**, 2200886.
10. M. Song, Z. Yi, R. Xu, J. Chen, J. Cheng, Z. Wang, Q. Liu, Q. Guo, L. Xie and C. Chen, *Energy Storage Materials*, 2022, **51**, 620-629.
  11. Y. Li, Y. Lu, Q. Meng, A. C. S. Jensen, Q. Zhang, Q. Zhang, Y. Tong, Y. Qi, L. Gu, M.-M. Titirici and Y.-S. Hu, *Advanced Energy Materials*, 2019, **9**, 1902852.
  12. R. Xu, Z. Yi, M. Song, J. Chen, X. Wei, F. Su, L. Dai, G. Sun, F. Yang, L. Xie and C.-M. Chen, *Carbon*, 2023, **206**, 94-104.
  13. C. J. Wen, B. A. Boukamp, R. A. Huggins and W. Weppner, *Journal of The Electrochemical Society*, 1979, **126**, 2258-2266.
  14. W. Weppner and R. A. Huggins, *Journal of The Electrochemical Society*, 1977, **124**, 1569-1578.
  15. Y. Zhu and C. Wang, *The Journal of Physical Chemistry C*, 2010, **114**, 2830-2841.
  16. K. Wang, Y. Xu, H. Wu, R. Yuan, M. Zong, Y. Li, V. Dravid, W. Ai and J. Wu, *Carbon*, 2021, **178**, 443-450.
  17. J. Xiang, W. Lv, C. Mu, J. Zhao and B. Wang, *J. Alloys Compd.*, 2017, **701**, 870-874.
  18. Z. Yang, H. Guo, F. Li, X. Li, Z. Wang, L. Cui and J. Wang, *Journal of Energy Chemistry*, 2018, **27**, 1390-1396.
  19. X. Lin, Y. Liu, H. Tan and B. Zhang, *Carbon*, 2020, **157**, 316-323.
  20. M. Yuan, C. Meng, A. Li, B. Cao, Y. Dong, D. Wang, X. Liu, X. Chen and H. Song, *Small*, 2022, **18**, 2105738.
  21. H. J. Oh, H. K. Kang, H. Ahn, J. Park, J. Choi, H. Y. Kim, E. Lee, S. Y. Yeo, Y. O. Choi, B. J. Yeang, S.-B. Son and B.-S. Lee, *Chem. Eng. J.*, 2023, **454**, 140252.
  22. H.-g. Sun, H.-h. Xiao, W. Song, J. Wang, W.-r. Zhang, S. Ru, Z.-q. Ai and C.-X. Wang, *J. Alloys Compd.*, 2019, **805**, 984-990.
  23. S. Alvin, H. S. Cahyadi, J. Hwang, W. Chang, S. K. Kwak and J. Kim, *Advanced Energy Materials*, 2020, **10**, 2000283.
  24. H. Kim, J. C. Hyun, D.-H. Kim, J. H. Kwak, J. B. Lee, J. H. Moon, J. Choi, H.-D. Lim, S. J. Yang, H. M. Jin, D. J. Ahn, K. Kang, H.-J. Jin, H.-K. Lim and Y. S. Yun, *Adv. Mater.*, 2023, **35**, 2209128.
  25. H.-Y. Yu, H.-J. Liang, Z.-Y. Gu, Y.-F. Meng, M. Yang, M.-X. Yu, C.-D. Zhao and X.-L. Wu, *Electrochim. Acta*, 2020, **361**, 137041.
  26. S. Qiu, L. Xiao, M. L. Sushko, K. S. Han, Y. Shao, M. Yan, X. Liang, L. Mai, J. Feng, Y. Cao, X. Ai, H. Yang and J. Liu, *Advanced Energy Materials*, 2017, **7**, 1700403.
  27. T. Chen, J. Zhang, Z. Wang, R. Zhao, J. He, J. Wu and J. Qin, *Energy*, 2020, **212**, 118771.

28. Y. Liu, M. Shi, M. Han, J. Yang, J. Yu, M. Narayanasamy, K. Dai, S. Angaiah and C. Yan, *Chem. Eng. J.*, 2020, **387**, 124104.
29. V. Selvamani, R. Ravikumar, V. Suryanarayanan, D. Velayutham and S. Gopukumar, *Electrochim. Acta*, 2016, **190**, 337-345.
30. X. Zhang, H. Qu, W. Ji, D. Zheng, T. Ding, C. Abegglen, D. Qiu and D. Qu, *ACS Applied Materials & Interfaces*, 2020, **12**, 11589-11599.
31. Y.-F. Du, G.-H. Sun, Y. Li, J.-Y. Cheng, J.-P. Chen, G. Song, Q.-Q. Kong, L.-J. Xie and C.-M. Chen, *Carbon*, 2021, **178**, 243-255.
32. X. Wang, J. Chen, C. Dong, D. Wang and Z. Mao, *ChemElectroChem*, 2022, **9**, e202101613.
33. N. Wang, Q. Liu, B. Sun, J. Gu, B. Yu, W. Zhang and D. Zhang, *Scientific Reports*, 2018, **8**, 9934.
34. M. Drews, J. Büttner, M. Bauer, J. Ahmed, R. Sahu, C. Scheu, S. Vierrath, A. Fischer and D. Biro, *ChemElectroChem*, 2021, **8**, 4750-4761.
35. A. Ramar, M. Sakthivel, F.-M. Wang and K.-C. Ho, *Carbon*, 2023, **213**, 118223.
36. Z. Liu, H. Peng, X. Xie, X. Wang, Y. Pu, G. Ma and Z. Lei, *J. Power Sources*, 2022, **543**, 231831.
37. N. Qin, L. Jin, Y. Lu, Q. Wu, J. Zheng, C. Zhang, Z. Chen and J. P. Zheng, *Advanced Energy Materials*, 2022, **12**, 2103402.
38. Y. Yang, C. Huang, R. Zhao, Z. Gao, X. Qi, W. Zhang, X. Lu, L. Qie and Y. Huang, *Journal of Materials Chemistry A*, 2023, **11**, 2947-2956.
39. J. Jiang, Y. Zhang, Z. Li, Y. An, Q. Zhu, Y. Xu, S. Zang, H. Dou and X. Zhang, *J. Colloid Interface Sci.*, 2020, **567**, 75-83.